Electronic Supplementary Material (ESI) for Nanoscale.

Electronic Supplementary Information: Fab on a Chip

Matthias Imboden[1], Han Han[2], Thomas Stark[3], Evan Lowell[4], Jackson Chang[1], Flavio Pardo[5], Cristian Bolle[5], Pablo G. del Corro[6], and David J. Bishop[1,2,4]

[1]*Department of Electrical and Computer Engineering*

[2]*Department of Physics*

[3]*Division of Materials Science and Engineering*

Boston University, Brookline, Massachusetts 02446, USA

[4]*Department of Mechanical Engineering*

Boston University, Boston, Massachusetts 02215, USA

[5]*Bell Labs, Alcatel-Lucent, 600 Mountain Avenue, Murray Hill, New Jersey 07974, USA*

[6]*Instituto Balseiro, Centro Atómico Bariloche, Bariloche Río Negro 8400, Republic of Argentina*

Table of Contents

1. Overview of MEMS Fabrication using PolyMUMPs

PolyMUMPs[1] is a surface micromachining process for creating MEMS devices via the deposition, patterning, and etching of thin layers on top of a substrate. The devices are composed of three polysilicon layers, two of which are moveable. Silicon dioxide acts as the sacrificial layers in between the polysilicon layers. In order of deposition, the layers consist of electrically isolating silicon nitride (0.6 µm), a fixed layer of polysilicon (0.5 µm), the first layer of oxide (2.0 µm), the first moveable device layer of polysilicon (2.0 µm), the second layer of oxide (0.75 µm), the second moveable device layer of polysilicon (1.5 µm), and a gold layer (0.5 µm). Following the manufacturing process, the moveable polysilicon layers are released through the etching of the sacrificial silicon oxide layers with hydrofluoric acid. The deposition of thin layers directly atop one another results in print-through of the patterning on all subsequent layers. Figure S1 shows the layers of PolyMUMPs and the conformal nature of the deposition. Minimum feature size and spacing is typically 2 µm.

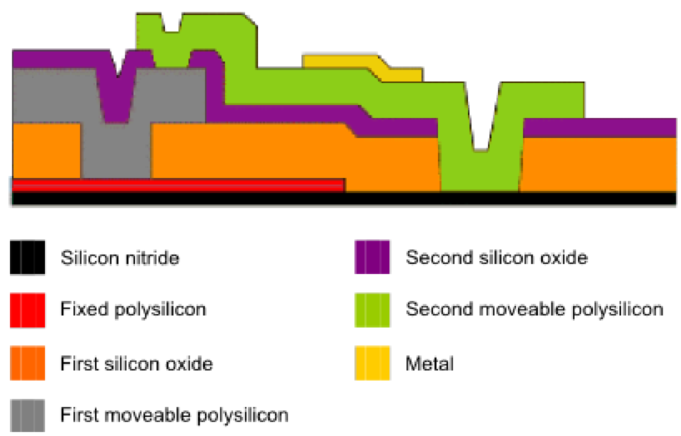

Figure S1. Cross-section view of the layers in PolyMUMPs, reproduced from reference [1].

2. Manufacturability of the Writers

The two step process of using the FIB to manufacture the apertures described in the main manuscript and detailed in [2], does not lend itself to large scale manufacturing. This is the only manufacturing step used in the work that is not based on a classical scalable lithography process. It is however conceivable, that a FIB based processing step could be integrated in a commercial foundry, resulting in low cost writers with submicron apertures.

We used the FIB in a two-step process. The initial pre-thinning and smoothing of the poly-silicon plate was accomplished using a rather high ion beam current of 500 pA. The milling time for the 4x4x1.2 µm^3 trough takes approximately 100 s. For the final apertures the beam current is reduced to 10 pA for the apertures with smallest features on the 200 nm scale and 1.5 pA for the apertures with features of 100 nm and below. For a simple circular aperture of these scales and geometry, the mill time is on the order of 20 s. It is not farfetched to use optical lithography and a well-timed RIE etch to create the troughs. In a subsequent step a 6” wafer containing 2600 writers can be loaded into a FIB. By optimizing the beam current and milling time, combined with image recognition software to guide the stage and located the troughs, each aperture could be milled in ~30 s. Like this the entire wafer containing 2600 writers would be processed in under 24 hours. While not entirely scalable in the classical sense, it is conceivable that production beyond prototyping is feasible. We use the FIB as it allows us full flexibility for prototyping and custom manufacturing.

Once a specific design and aperture is chosen there are other, non-FIB based methods available to produce sub-micron pores. For example, a UV-lithography step could be used to build larger apertures that are then filled in using controlled deposition techniques such as atomic layer deposition. While some of the customization flexibility is lost, such an approach is scalable and could significantly reduce the time and cost to produce the writers.

3. Optical Displacement Calibration using Digital Image Correlation

Digital Imaging Correlation (DIC) techniques are used to calibrate the electromechanical response of the MEMS writers. This can be achieved with digital image processing software based on MATLAB. For this analysis optical images are taken at magnification of 200x or 1000x while actuating the MEMS combs. By comparing two images, voltage biased and unbiased, this technique allows for sub-pixel accuracy in the determination of the mechanical displacement surface. The two images correspond to a reference (or unformed, $V = 0$) image, labeled A, and a shifted (or deformed, $V > 0$) image, labeled B. There are many different methods to achieve sub-pixel resolution. Reference [3] analyzes the performance of three approaches commonly used in sub-pixel registration algorithms. Reference[4] demonstrates the application of such methods for a MEMS device similar to the writers discussed here. The DIC algorithm used is the correlation coefficient calculation and curve fitting method described in reference [5] is performed as follows.

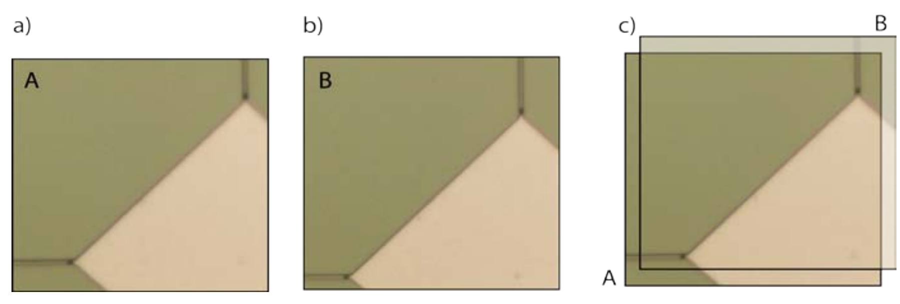

Figure S2. a) Images A and B with displaced writer plate. b) Shift of B respect to A needed for both images to overlap. A is the reference image and B the image taken at a given voltage (V>0).

The deformed image is displaced in a 2D surface with respect to the reference image, as depicted in Figure S2. A correlation coefficient r, defined by equation (S1), is calculated for each displacement. Changing the displacement along the two axes of a plane generates a surface of correlation coefficients, an example of which is shown in Figure S3. r is calculated using the corr2 MATLAB function:

$$r = \frac{\sum_m \sum_n (A_{mn} - \bar{A})(B_{mn} - \bar{B})}{\sqrt{\left(\sum_m \sum_n (A_{mn} - \bar{A})^2\right)\left(\sum_m \sum_n (B_{mn} - \bar{B})^2\right)}} \tag{S1}$$

A and B are the matrices of the reference and the shifted image respectively, where each element in the matrix is the greyscale value of the corresponding pixel (typically ranging from 0 for white to 255 for black). $\bar{A}$ and $\bar{B}$ are the mean values for matrix A and B, respectively, where $\bar{A} = \sum_{i,j}^{n} \frac{A_{ij}}{n^2}$.

Two equal images correspond to the highest possible correlation making r = 1, and any discrepancy will reduce the value of r. Therefore the maximum value in the correlation surface indicates the spatial displacement, given in pixels, at which the two images are most similar, *i.e.* it determines how many pixels image B must be moved in order to overlap with image A as show in Figure S2 b). This then corresponds to the displacement caused by applying an actuation voltage.

To obtain sub-pixel accuracy for the maximum r, the correlated surface can be fitted to a second order polynomial in the vicinity of the maximum (Figure S3 b))

$$f(x, y) = a_1 + a_2 x + a_3 y + a_4 x^2 + a_5 yx + a_6 y^2 \tag{S2}$$

The maximum is found at the x and y coordinates given by

$$\begin{aligned} y_{max} &= \frac{-2\, a_3\, a_4 + a_5\, a_2}{4\, a_4\, a_6 - a_5^{\,2}} \\ x_{max} &= \frac{-2\, a_6\, a_2 + a_5\, a_3}{4\, a_4\, a_6 - a_5^{\,2}}. \end{aligned} \tag{S3}$$

The coordinates of the maximum of this fitted surface, given by equation (S3), multiplied by a scaling factor that relates pixels to distance, determines the displacement of the two images and hence the displacement of the MEMS device.

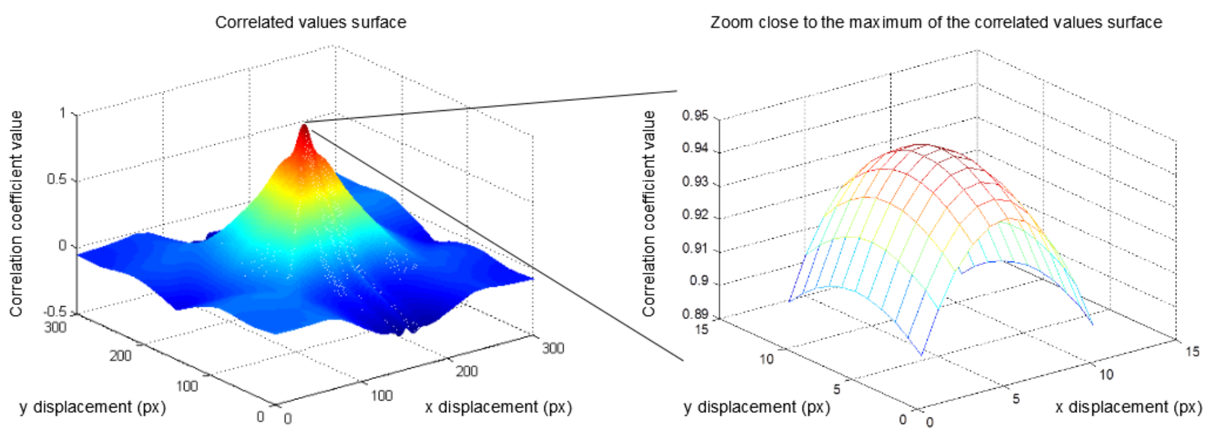

Figure S3. a) plot of a surface of the correlated values r between a reference image and another image shifted by (x,y) pixels. b) A close up of the maximum made up of 10 by 10 pixels is used for the polynomial surface fit.

The MEMS devices can be calibrated along each axis independently. The simultaneous actuation of two combs measures the mechanical coupling between axes. An example of this is illustrated in Figure S3, where the DIC algorithm was used to calculate the displacement of a device actuated along the negative y-axis. The red data points plot the displacement versus V^2. Each image was taken at a magnification of 1000x corresponding to a pixel size of 50 nm. A 10 by 10 pixel matrix covering the maximum was used to make the fitted surface and calculate the displacement at each applied voltage. The standard displacement error, based on the error of the fitting parameters, is on the order of 2.5 nm for one-sigma (standard deviation) confidence interval. This corresponds to 0.05 pixel resolution.

The black line in Figure S4 is a fit assuming the standard electromechancial coupling for linear comb-spring structures, given by

$$x = \frac{1}{2k}\frac{dC}{dx}V^2, \tag{S4}$$

where k is the spring constant and dC/dx is the variation of the comb-drives' capacitance with respect to position. The linear fit is a measure of the electromechancial coupling $\frac{1}{2k}\frac{dC}{dx} = (-1.41 \pm 0.01)\ {}^{\mathrm{nm}}/_{\mathrm{V}^2}$. Each axis results in a calibration value used to determine the voltages needed for the MEMS writers to trace a desired pattern. The resulting displacement accuracy depends on the size of a pixel for a given image (magnification), as well as image attributes including brightness, contrast, focus, and also mechanical noise such as vibration and stability of the microscope stage.

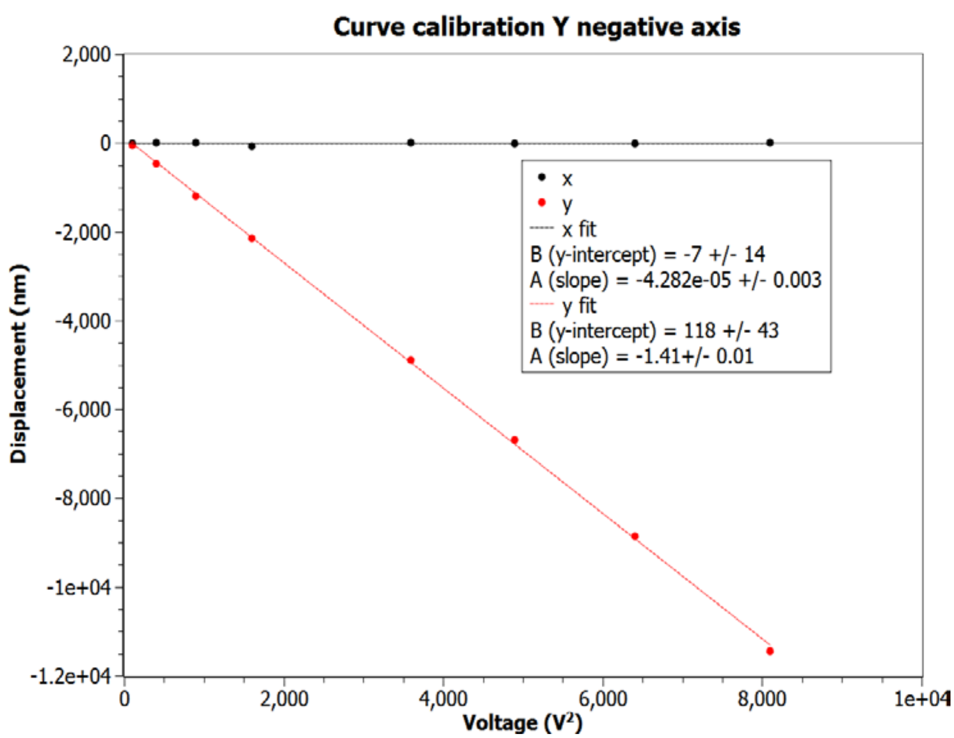

Figure S4. Displacement vs. voltage squared of the writer along the negative y-axis. All other combs are set to ground. The dots in black and red are the displacements for each voltage along the x- and y axis respectively. Solid traces are linear fits to equation (S4).

4. Atomic Micro Sources

Figure S5 shows the atomic flux as a function of temperature for zinc, lead, indium, gold, iron, and silicon, calculated from the Hertz-Knudsen equation[6] (equation (2) in the main manuscript). The figure shows that Zn, Pb, In, Au, and Fe are some of the materials for which a flux of at least 10^3 atoms/s-μm^2 can be generated at temperatures well below 1683 K, the melting temperature of the silicon hotplate, making them candidates for use in our FoC system. Figure S5 further shows that the partial pressure imposes a cutoff to the lowest flux that can be obtained; for nonzero partial pressures, the atomic flux is rapidly suppressed at this cutoff. This emphasizes the importance of conducting evaporations under ultra-high vacuum conditions, such as those typically found in a cryostat, where the partial pressure is lower than the saturated vapor pressure, even at fairly low evaporation temperatures.

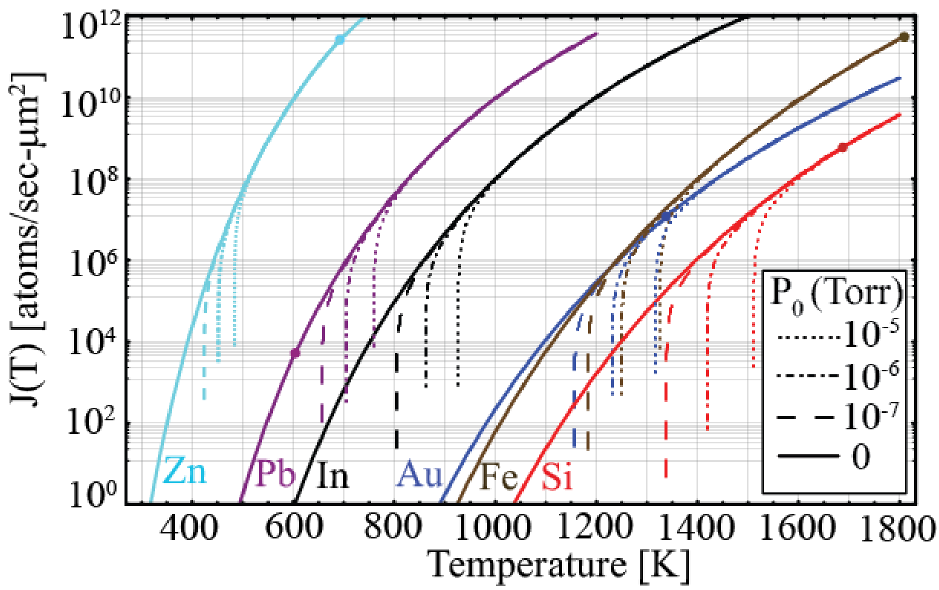

Figure S5. Plot of atomic flux as a function of temperature, for partial pressures ranging from 0 to 10^{-5} Torr, for select materials, calculated from the Hertz-Knudsen equation (equation (2) in the main manuscript). The fluxes at the melting points are indicated with dots.

The temperature of the evaporating indium and hence silicon plate can be estimated using the SEM images shown in Figure 7 of the main manuscript. In Figure 7 a) at time t = 0 s, the polysilicon plate has an approximately uniform layer of indium. When the plate is resistively heated by applying a voltage, the indium melts and balls up (Figure 7 b)) and evaporates (Figure 7 c)) until the indium is exhausted (Figure 7 d)). Between b) and c) the power is ramped from $P \approx 11$ mW to $P \approx 27.5$ mW, as shown in Figure S6. We considered the evaporation of indium to be from the upper surface of a hemisphere of radius r, between approximately 917 s and 1253 s, as shown in Figure S6 c) and d). The volume of the hemisphere decreases at a rate proportional to the area A of its upper surface:

$$\frac{dV}{dt} = J(T) A\, v, \qquad \text{(S5)}$$

where $J(T)$ is the atomic flux (atoms/s-μm^2) of indium at temperature T and v is the volume occupied by a single indium atom in the condensed state. Taking the time derivative of the volume of a hemisphere and equating it to (S5) results in an expression that relates the rate of change in radius to the atomic flux,

$$\frac{dV}{dt} = A\, \frac{dr}{dt} = J(T) A\, v\ ,$$

or

$$J(T) = \frac{1}{v}\frac{dr}{dt}. \qquad \text{(S6)}$$

From the images, we determined a value of $dr/dt \approx 0.06$ μm/s which, according to equation (S6), corresponds to a flux of $\sim 10^9$ atoms/s-μm^2. From the Hertz-Knudsen equation, for a partial pressure of 10^{-5} Torr, a flux of $\sim 10^9$ atoms/s-μm^2 corresponds to a temperature of $\sim$1100 K. As previously discussed, the heaters fail when the applied power exceeds 36 mW (t = 2079 s). The failure is believed to occur at a temperature below 1683 K, the melting point of silicon, thought to be caused by thermal stress-induced cracking.

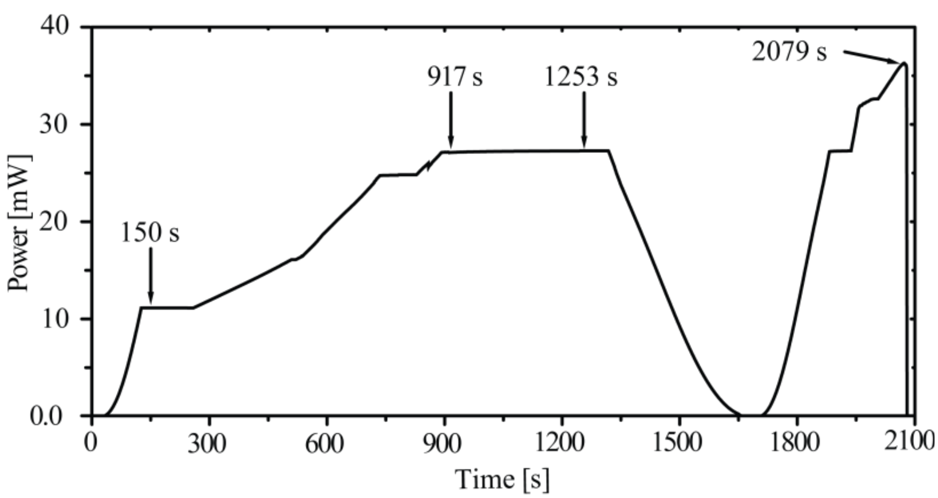

Figure S6. Power dissipated by the hotplate during the evaporation of indium in an SEM.

5. MEMS Plates as Atom Velocity Filters

Using two overlapping plates, an atom velocity filter can be implemented. A diagram of one possible configuration and the resulting atom speeds are depicted in Figure S7. A flux of atoms passes through an aperture of diameter d in polysilicon plate 1, which is moving at velocity v_P. Atoms moving faster than the cutoff speed v_{max} in Figure S7 will strike plate 2, before the aperture arrives at their location, those traveling slower than v_{min} will strike the plate 2 after the aperture has already passed. Only those with speeds in between v_{min} and v_{max} will pass through both apertures. v_{min} and v_{max} are plotted for two plate separations h, as a function of the relative plate displacement. Each plate is t =1.5 μm thick. It is assumed that the plate velocities are the same, v_P = 1 m/s. Each plate has a finite thickness t, resulting in a minimum speed required for the atoms to pass a single plate $v_{min,P} = t/d \times v_P$. The incoming atom flux speeds have a Maxwell distribution[7], hence there will always be some slow moving atoms that can be selected. As the plots indicate, having a larger plate separation h allows for considerable tuning with a relatively narrow range of velocities that can pass for a given plate alignment and velocity.

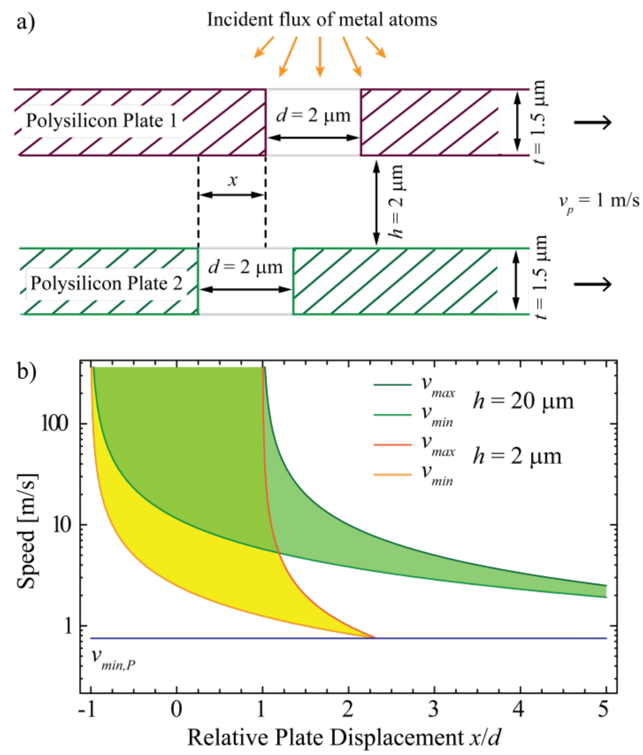

Figure S7. Velocity filter. a) Diagram of two overlapping plates with large apertures. Both plates are moving at velocity v_p = 1m/s. b) Max and minimum speed of atoms that can pass both plates. The x axis indicates the relative position of the two plates. The shaded region indicated allowed speeds.

6. MEMS Mass Sensor

6.1 Modeling the MEMS mass sensor

The mass sensor was modeled in 3D using CAD software with the same design parameters as the MEMS design. The 3D model was then imported into COMSOL for eigenfrequency simulation. To mimic material deposition, a mass loading boundary condition was applied to the upper surface of the center plate, within the same area as the shield opening. When using a mass loading boundary condition, mass is added without changing the stiffness of the structure. This approximation is only valid if the added material does not contribute significantly to the spring constant of the device. The assumption holds for three reasons: 1) many metals used for deposition, such as gold, have much higher densities and lower Young's moduli than silicon, making the mass contribution to the resonance shift dominate the mechanical contribution; 2) the spring constant of the device is determined predominantly by the folded spring, while all the added mass can contribute to the mass change; 3) no tension can exist in the deposited film because, for the thickness range of interest, the deposited film is not continuous due to the fact that the surface roughness of the polysilicon is on the order of 10 nm.

Though most of the spring constant is provided by the folded spring, the oscillating plate itself may also bend on resonance, causing the plate to curve. The concept of effective mass is exploited to better model the spring-mass system. For any real resonator, the mass along the length of the spring has a distribution in amplitude. The effective mass is a measure of the relative displacement of each infinitesimal mass unit, and can be defined as followed:

$$\iiint \frac{1}{2}\, v^2\, dm = \iiint \frac{1}{2}\, \rho\, v^2\, dV = \frac{1}{2}\, m_{eff}\, {v_{max}}^2. \tag{S7}$$

The LHS is the total kinetic energy of the oscillation system. The RHS is the kinetic energy of a point mass with a velocity the same as the maximum velocity for all points of the oscillating system. The effective mass is mode dependent and always smaller or equal to the true mass. The effective mass of the deposited thin film Δm_{eff} can be defined in the same way, where in this case the integral runs over the volume of added mass, not the entire resonator. As discussed previously, the spring constant of the system will not be affected by the added mass, therefore, for a small added mass (small compared to the total mass of the resonator), a simple relationship between the effective mass change and resonant frequency can be used:

$$\frac{\Delta f}{f} = -\frac{1}{2}\frac{\Delta m_{eff}}{m_{eff}} \tag{S8}$$

The effective mass of the mass sensor m_{eff} can be easily calculated by integrating over the volume of the resonator:

$$m_{eff} = \rho \iiint \left(\frac{v}{v_{max}}\right)^2 dV = 0.8013\, m_0 = 1.354 \times 10^{-10}\ \text{kg}. \tag{S9}$$

Here, $m_0 = 1.690 \times 10^{-10}$ kg is the mass of the mass-spring system in the simulation, including the oscillating plate and the folded springs. v/v_{max} is determined by oscillation geometry assuming that, for a small amplitude oscillation, each point of the system is undergoing a harmonic oscillation with the same frequency. Thus the ratio of velocities between two different locations is equal to the ratio of the amplitudes.

The effective mass of the deposited film Δm_{eff} for a given actual mass Δm is also obtained by taking the surface integral over the area of the shield opening on the oscillating plate. Assuming a uniform thickness, we get

$$\Delta m_{eff} = \frac{\Delta m}{A} \iint \left(\frac{v}{v_{max}}\right)^2 dS = 0.8581\, \Delta m, \qquad \text{(S10)}$$

where A is the area of the shield opening. The ratio between Δm_{eff} and Δm stays constant for varying Δm because it depends entirely on the geometry and oscillation mode of the mass sensor. In this case, by combining this ratio into m_{eff}, equation (S8) can be rewritten as

$$\Delta m = -2 \cdot m_{ce} \cdot \frac{\Delta f}{f}, \qquad \text{(S11)}$$

where m_{ce} is the combined effective mass. $m_{ce} = \frac{1.354\times10^{-10}\ \text{kg}}{0.8581} = 1.578 \times 10^{-10}$ kg.

The simulated frequency shift for an added mass boundary condition of the fundamental mode is plotted in Figure S8. The fit confirms the linear relationship between the frequency shift and change of effective mass with a slope of -0.4956 ± 0.0004, which is close to the theoretical prediction of -1/2. The intercept is -9.42 ± 2.37 x 10^{-6}. The fitting line, together with equations (S9) and (S10), is the basis of measuring mass of change by monitoring frequency shift. It should be noted that the linear relationship only holds within a certain regime because, for large mass change, the accurate form of the frequency shift is

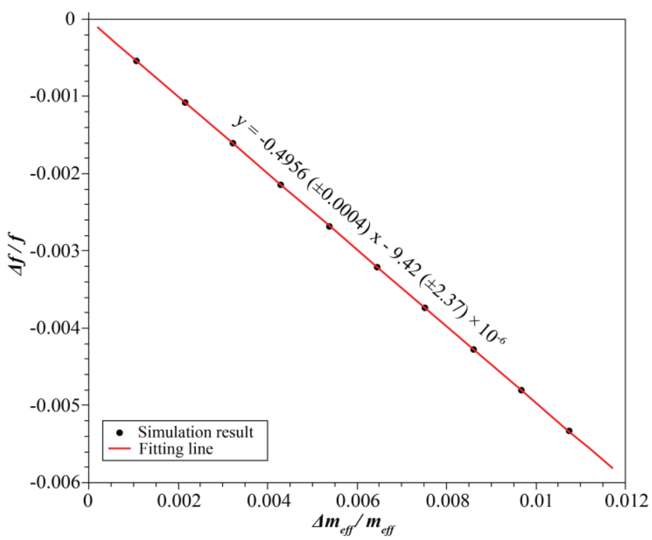

Figure S8. The simulation of mass loading effect on the mass sensor shows a linear relationship between the frequency shift and change of effective mass.

$$\Delta f = \frac{1}{2\pi}\sqrt{\frac{k}{m+\Delta m}} - f_0 \qquad \text{(S12)}$$

In our application, we are only interested in the regime where the assumption of linear dependency offers adequate accuracy.

6.2 Driving and sensing the MEMS mass sensor

The MEMS mass sensor is capacitively driven and sensed. When applying a voltage across the two plates of the resonator, the equation of motion for the oscillating plate can be written as

$$\ddot{x} + \gamma\dot{x} + \frac{k}{m}x = \frac{1}{2m}\frac{dC}{dx}V^2 \tag{S13}$$

For small amplitude oscillation, the capacitance of the resonator can be approximated as

$$C = C_0 + C'x + C''x^2, \tag{S14}$$

where C_0 is the capacitance at the equilibrium position while C' and C'' are the first and second derivatives of the capacitance evaluated at the equilibrium position. The driving voltage is a superposition of AC and DC signals, so by plugging equation (S14) into the equation of motion, one can get

$$\ddot{x} + \gamma\dot{x} + \frac{k}{m}x = \frac{1}{2m}(C' + 2C''x)(V_{dc} + v_{ac})^2 \tag{S15}$$

Since the amplitude of the AC signal v_{ac} is much smaller than the DC bias V_{dc}, to a first order approximation, equation (S15) can be simplified as

$$\ddot{x} + \gamma\dot{x} + (\frac{k}{m} - \frac{C''{V_{dc}}^2}{m})x = \frac{1}{2m}C'{V_{dc}}^2 + \frac{1}{m}C'V_{dc}v_{ac}. \tag{S16}$$

For a harmonic excitation $v_{ac} = v_i \cdot \cos\omega t$, by redefining the equilibrium position of *x*, this equation can be solved and the solution is

$$x(t) = A(\omega)\cos\big(\omega t + \varphi(\omega)\big), \tag{S17}$$

with

$$A(\omega) = \frac{\frac{1}{m}C'V_{dc}v_i}{\sqrt{(\omega^2 - {\omega_0}^2)^2 + \gamma^2\omega^2}}\ ,\ \ {\omega_0}^2 = \frac{k}{m} - \frac{C''{V_{dc}}^2}{m}, \tag{S18}$$

and

$$\varphi(\omega) = \tan^{-1}\frac{\gamma\omega}{{\omega_0}^2 - \omega^2} \tag{S19}$$

The oscillation is sensed by detecting the current flowing from the static plate

$$i = -\frac{dQ}{dt} = -\frac{d[(C_0 + C'x + C''x^2)(V_{dc} + v_{ac})]}{dt} \approx -V_{dc}C'\frac{dx}{dt} - C_0\frac{dv_{ac}}{dt} \tag{S20}$$

The second term has an amplitude linearly dependent on ω, while the first term depends strongly on ω near ω_0

$$i = \frac{\frac{1}{m}\left(C'V_{dc}\right)^2 v_i\omega}{\sqrt{(\omega^2 - {\omega_0}^2)^2 + \gamma^2\omega^2}}\sin\big(\omega t + \varphi(\omega)\big) + C_0 v_i\omega\sin(\omega t), \tag{S21}$$

which indicates the current has a Lorentzian line shape for a frequency sweep near ω_0, after subtracting out the background term $C_0 v_i\omega\sin(\omega t)$.

6.3 Circuit setup for the MEMS mass sensor

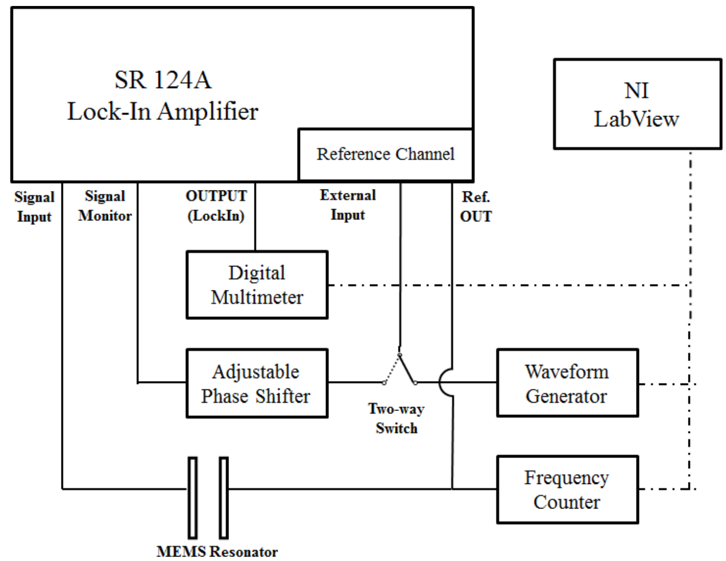

Figure S9. The circuit diagram of MEMS resonator self-oscillating

In order to monitor the atomic flux during an experiment, the resonance frequency is continuously monitored. To this end, a self-oscillating circuit was built using a SR 124A Lock-in amplifier to complete the phase-locked loop. The circuit diagram is shown in Figure S9. The Lock-in amplifier uses a reference channel to lock onto the external signal, and outputs a sinusoidal signal with the same frequency as the reference. The output signal is used to drive the resonator and the signal sensed on the ground plate of the resonator is sent back to the Lock-in amplifier to form a closed resonating loop. The AC amplitude, phase and DC bias of the output signal can be set to desired values on the front panel. A frequency counter is used to measure the resulting closed loop resonance. The averaging time for frequency counting is 0.5 seconds, followed by 0.5 seconds of data communication and processing time.

Such a system can work as either an open loop setup using a waveform generator as the frequency source or closed loop to form a self-oscillating circuit. With the open loop setup, the resonator can be characterized by performing a frequency sweep to get the Lorentzian response. Figure S10 shows the plot of such a sweep. In the sweep, the driving voltage is set to 10 mV with a DC bias of 500 mV. The y-axis is the amplified current sensed on the ground plate of the resonator with the sensitivity of the Lock-in amplifier set to 1 nA. For a harmonic oscillator with a damping proportional to the velocity, the oscillation amplitude should have a Lorentzian line shape according to the discussion above

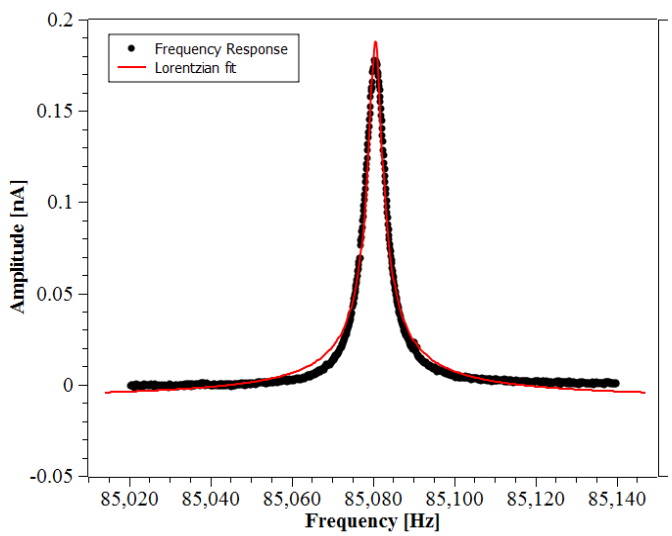

Figure S10. The Lorentzian response of an 85 kHz resonator. The Q-factor of this resonator is around 26K.

$$u(f) = \frac{\frac{u_{max} \cdot f_0}{Q} f}{\sqrt{(f^2 - {f_0}^2)^2 + (\frac{f \cdot f_0}{Q})^2}},$$

where $u(f)$ is the oscillation amplitude depending on frequency; u_{max} is the oscillation amplitude at resonance; f_0 is the resonant frequency; Q is the quality factor, which describes the width of the resonance peak. A curve fitting using this equation has been applied to the sweep data. The fit gives $f_0 = 85080.664 \pm 0.013$ Hz and $Q = 26442 \pm 258$.

For a closed loop oscillation, the oscillating frequency in the loop will be locked to the resonator's resonant frequency. In a mass loading experiment, the resonant frequency shifts due to the mass change, but the oscillating frequency will be shifted as well to follow the resonant frequency at all times. By reading the frequency counter, the added mass can be easily calculated using equation (S11) above or calibrated by a macroscopic film thickness monitor typically used in thin film deposition systems. For such a phase-locked state, the typical AC driving voltage is 10 to 20 mV, with a DC bias voltage of 100 to 500 mV for a 85 kHz mass sensor.

6.4 Stability and sensitivity of the MEMS mass sensor

The advantage of self-oscillating phase-locked-loop is that it provides an extremely precise real-time measurement of resonant frequency, which strongly depends on the mass loading. The resolution and precision of this measuring system is determined by the stability of the measured frequency that can be quantified. Allan deviation is a widely used two-sample deviation to evaluate the frequency stability of oscillators[8]

$$\sigma_f(\tau) = \sqrt{\frac{1}{2N}\sum_{n=1}^{N\to\infty}\left(\bar{f}_{n+1} - \bar{f}_n\right)^2}, \tag{S23}$$

where τ is the averaging time for each measurement; $\bar{f}_n$ is the average value of the n-th measurement. Also the definition of Allan deviation is based on measurements which have no wait time between them. Since, in our current setup, a wait time is used for data processing and communication, the Allan deviation is obtained by applying a conversion to eliminate the influence of wait time[9].

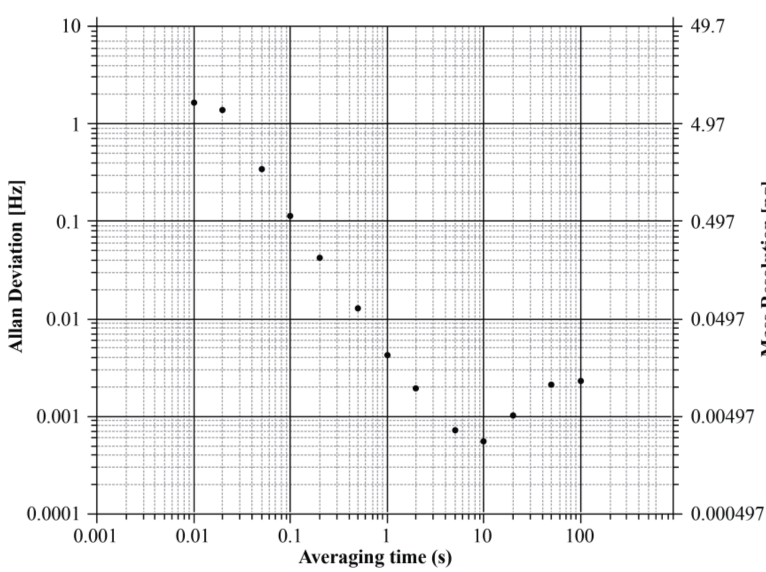

Figure S11. The Allan deviation of an 85 kHz mass sensor for different averaging time, demonstrating ~1:10^8 resolution. This measurement is done on a different sample other than the one discussed in the main text.

The Allan deviation of the mass sensor for different averaging time has also been measured. The result is shown in Figure S11. The minimum of Allan deviation occurs at $\tau = 10$ s. $\sigma_f(\tau = 10 \text{ s}) = 0.717$ mHz. However, when using the mass sensor as a film thickness monitor during evaporation, a fast response of the mass change is desired. Hence for our application the averaging time is determined as a balance of both resolution and response time.

7. Mass Transfer from Source to Sensor; Temperature Estimate of the Micro-Source

Using the MEMS mass sensor, we calculated the mass deposited on the resonator that originated from a micro-source. The mass deposited on the plate as a function of time *m(t)* is determined in this way. As shown in Figure 10 of the main manuscript, dm/dt takes on distinct values during various time intervals of the evaporation. We used a linear fit to determine the value of dm/dt on each interval. Knowing the area A of the resonator plate and the mass if the indium atom m_{In}, we calculated the flux J_R incident onto the resonator

$$J_R = \frac{dm}{dt}\frac{1}{m_{In}}\frac{1}{A} \tag{S24}$$

Assuming that the source flux has the same angular dependence as a Knudsen cell, we considered geometric factors to determine the flux J_S emitted from the source. The flux values range from 7.8×10^5 to 1.2×10^8 atoms/ sec · μm^2. Using the Hertz-Knudsen equation (equation (2) in the main manuscript) for a partial pressure $P_0 = 10^{-5}$ Torr, the fluxes correspond to temperatures ranging from 928-1009 K. These numbers are consistent with the powers applied to the micro-source and the temperatures and evaporation rates determined from the SEM images presented in the main manuscript.

8. Making Electrical Contact using Polysilicon Leads

Figure S12 shows a non-ohmic I-V curve of a series circuit consisting of two polysilicon leads and two polysilicon-platinum junctions connected face to face by a thermally deposited indium bridge. For the sample measured, the resistance of a single polysilicon lead is calculated to be 1.6 kOhm based on the geometry of the lead design and the resistivity of doped silicon[1]. The total circuit resistance is higher than 3.2 kOhm (two leads in series), as it includes the resistance of the indium trace and the contact resistance between platinum and silicon leads, which can be modeled as a metal-semiconductor junction. For such a junction, the current-voltage relationship is formulated as[10]

$$I = I_0(e^{\frac{V}{V_0}} - 1), \tag{S25}$$

where I_0 and V_0 are fitting parameters to be determined from the data. To simplify the problem, the metal-semiconductor junction is considered ohmic for reverse bias voltage. By taking all ohmic components of the circuit into account, the final form of the fitting function can be written as

$$V = V_0 \, log\left(\frac{I}{I_0} + 1\right) + I \cdot R \quad (I > 0), \tag{S26}$$

where R is the total ohmic resistance including leads, indium bridge and the reverse biased junction.

A least squares curve fit to the $I > 0$ part of the data yields I_0 = 27.8 ± 0.2 μA, V_0 = 0.521 ± 0.003 V and R = 4756 ± 13 Ohm, with a very high correlation coefficient of 0.999997. The fitting for the $I < 0$ part of the data gives similar results. Both data and fitting curves are presented in Figure S12. Though the diode model can interpret the electrical behavior of the lead system to some degree, more studies are to better understand the values of parameters and relate them to the band structure of the junction.

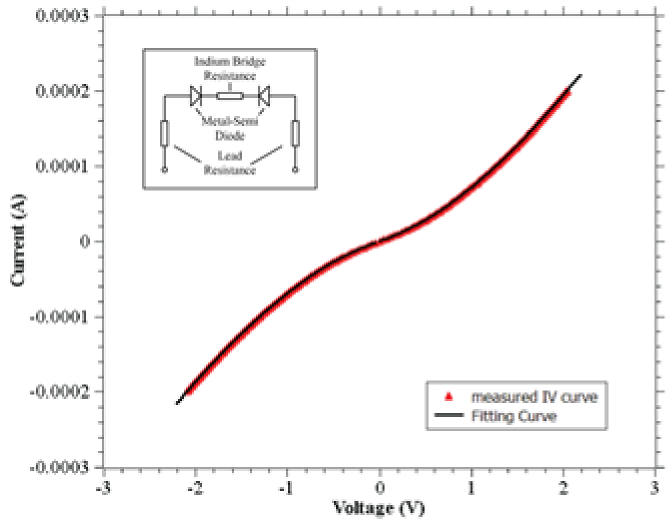

Figure S12. *I-V* measurement plot of the two-lead system and the corresponding fitting curves. The inset is the equivalent circuit diagram.

References

1 A. Cowen, B. Hardy, R. MahadevanandS. Wilcensk, *MEMSCAP,* 2013,

2 M. Imboden, H. Han, J. Chang, F. Pardo, C. A. Bolle, E. Lowell, and D. J. Bishop, *Nano Letters,* 2013, **13,** 3379.

3 P. Bing, X. Hui-min, X. Bo-qin, and D. Fu-long, *Measurement Science and Technology,* 2006, **17,** 1615.

4 X. Liu, K. Kim, and Y. Sun, *Journal of Micromechanics and Microengineering,* 2007, **17,** 1796.

5 P. Hung and A. Voloshin, *Journal of the Brazilian Society of Mechanical Sciences and Engineering,* 2003, **25,** 215.

6 MW Roberts and CS McKee. *Chemistry of the metal-gas interface,* Oxford Univ. Press, Oxford, 1978.

7 D. Mattox and J. McDonald, *Journal of Applied Physics,* 1963, **34,** 2493.

8 D. W. Allan, *Proceedings of the IEEE,* 1966, **54,** 221.

9 J. A. Barnes and D. W. Allan, *NIST Technical Note,* 1987, **1318,** 227.

10 R. Tung, *Physical Review B,* 1992, **45,** 13509.